ELSEVIER

Contents lists available at ScienceDirect

# **Applied Food Research**

journal homepage: www.elsevier.com/locate/afres





# Rapid and non-destructive monitoring of the drying process of glutinous rice using visible-near infrared hyperspectral imaging

Kabiru Ayobami Jimoh <sup>a</sup>, Norhashila Hashim <sup>a,b,c,\*</sup>, Rosnah Shamsudin <sup>d</sup>, Hasfalina Che Man <sup>a,b,c</sup>, Mahirah Jahari <sup>a,b</sup>

- <sup>a</sup> Department of Biological and Agricultural Engineering, Faculty of Engineering, Universiti Putra Malaysia, 43400 Serdang, Selangor, Malaysia
- <sup>b</sup> SMART Farming Technology Research Centre, Faculty of Engineering, Universiti Putra Malaysia, 43400 Serdang, Selangor, Malaysia
- Institute of Aquaculture and Aquatic Sciences (I-AQUAS), Universiti Putra Malaysia, Batu 7, Jalan Kemang 5, Negeri Sembilan, Port Dickson 70150, Malaysia
- d Department of Process and Food Engineering, Faculty of Engineering, Universiti Putra Malaysia, 43400 Serdang, Selangor. Malaysia

#### ARTICLE INFO

# Keywords: Grain quality Dehydration Computational intelligence Non-destructive method Hyperspectral imaging

#### ABSTRACT

Rapid and non-invasive monitoring of the drying process of glutinous rice is crucial to ensure the effective production of desired dried grain. In this study, visible-near infrared hyperspectral imaging coupled with computational intelligence was used to detect the variation in moisture content (MC), change in colour ( $\Delta E$ ), and golden index (GI) of glutinous rice during drying. Different preprocessing methods and effective wavelength selection techniques were used to eliminate the noise and redundant wavelength in the reflectance spectra, and predictive models were developed for the glutinous rice quality. Savitzky-Golay first derivative (SG1D) showed the best preprocessing performance (0.9564  $\leq R_P^2 \leq 0.9781$ , 0.0177  $\leq RMSEP \leq 0.8242$  and 1.28  $\leq MAPD \leq 5.90$  for PLSR model). The best performance accuracy ( $R_P^2 \geq 99.99$ ) was obtained when the SG1D and Gaussian process regression (GPR) model were combined with iteratively retained informative variable algorithm (SG1D-IRIV-GPR), variable iterative space shrinkage (SG1D-VISSA-GPR) and variable combination population analysis (SG1D-VCPA-GPR) for the prediction of MC, GI, and  $\Delta E$ , respectively. The study showed that visible-near infrared hyperspectral imaging coupled with computational intelligence can be used to monitor the quality of glutinous rice during the drying process.

#### 1. Introduction

Rice is an extensively consumed plant-based staple food. It offers more than half of the daily calories required for feeding the world population and up to two-thirds in Asia (Shi et al., 2022). Numerous varieties of rice differ in terms of physical characteristics, chemical composition, and textural and structural attributes, among other quality factors (Qiu et al., 2021). Glutinous rice, sometimes called sticky rice or waxy rice, is a popular variety of rice frequently grown in Eastern and Southeast Asia. The low amylose and high amylopectin content of glutinous rice kernel, as opposed to non-glutinous rice, accounts for its low retrogradation rate and high stickiness after cooking (Jimoh et al., 2025a, 2025b). The kernels of wet or freshly harvested glutinous rice are translucent in colour and become opaque after drying. This phenomenon differs entirely from non-glutinous rice, which turns translucent after drying (Li et al., 2018). Glutinous rice remains the main ingredient

in making many Asian staple foods, snacks, desserts, and beverages (Li et al., 2018; Qiu et al., 2021), which include rice wine, crackers, cakes, and dumplings (Qiu et al., 2020). Before the production of final products, fresh glutinous rice usually has a high moisture content (MC), which can be detrimental to its shelf life and quality, just like every other grain. Therefore, the grain is dried to a safe moisture level (9–14 %) before subjecting it to further processes such as storage, packaging, milling, and grinding (Jimoh et al., 2023a).

Drying refers to using hydrodynamic and thermodynamic methods to remove moisture by evaporation (Mondal et al., 2022). In practice, effective drying is crucial to the nutrients retained in dried products as the grains with incomplete drying are prone to mould growth, while over-dried grains are prone to nutrient loss (Jimoh et al., 2024b; Kiani et al., 2018). Therefore, the MC and physical appearance of the grains are monitored as effective metrics to control and terminate the drying process when the desired safe limit is attained (Jimoh et al., 2023b). The

E-mail address: norhashila@upm.edu.my (N. Hashim).

<sup>\*</sup> Corresponding author.

traditional methods for determining MC include the gravimetric method, Karl Fisher titration, infrared moisture analysers, and the standard oven drying method. When used correctly and meticulously, these traditional methods are accurate and dependable (Zhang et al., 2022). Nonetheless, they are destructive and require a lot of labour and time, mainly when dealing with many samples (Zhang et al., 2023a). The appearance of glutinous rice during drying is also an essential metric for grain processors and consumers during processing and procurement. The potential consumers of the product are often fond of comparing the golden appearance of the dried grains from different suppliers. The consumers associate the golden appearance of the grains with the nutrient retention, shelf life, and quality of the dried grain. This expectation is also transferred to the quality of the finished product obtained from the grain Iheonye et al. (2019). Conventionally, the appearance of the grains after drying is obtained using a colourimeter, and this technique can be time-consuming due to repeated measures. Also, it requires direct contact with the sample as it was primarily developed for flat surfaces, unlike the ellipsoid surface of rice, which makes it prone to some level of uncertainty. Thus, a highly efficient, low-cost, rapid, drudgery-free, and accurate quality evaluation method for rapid quality control and measurement during the drying process must be developed (Ren et al., 2020; Zhang et al., 2023a). Hyperspectral imaging (HSI) is an evolving, rapid, and non-invasive technique for monitoring food quality. It combines imaging and spectral technology to achieve the purpose of food quality detection (Jimoh et al., 2023b). In HSI techniques, a single captured image contains spatial information at every wavelength and spectral information in each pixel. The HSI has an advantage over the RGB camera by using a wide range of wavelengths, allowing it to detect the chemical and internal quality of the sample (Guo et al., 2023a; Sharma et al., 2022; Song et al., 2023). HSI technology has been widely applied in different food quality detection, assessment, control, and monitoring scenarios. For instance, the technology has been used in food testing, such as moisture, starch, and protein of wheat flour (Zhang et al., 2023a), moisture, starch, and protein of chicken flesh (He et al., 2023), and lead content of rape leaf (Zhou et al., 2023). Also, it was employed to detect chemical and biological traits in grain, which includes sweet seed vigour (Zhang et al., 2023b), aflatoxin B<sub>1</sub> and total aflatoxin in peanut kernel (Guo et al., 2023a), aflatoxin in corn kernel (Tao et al., 2022), the protein content of chickpea (Saha et al., 2023), amylose and amylopectin content of sorghum (Huang et al., 2021, 2023), corn physical traits and protein composition (Varela et al., 2022), hardness of maize kernel (Qiao et al., 2022), fatty acid and moisture content of rice (Song et al., 2023), and MC in soybeans (Guo et al., 2023b). However, the information on the application of the HSI system for monitoring the grain drying process remains a gap that demands research attention. Therefore, this study focused on developing a rapid and non-invasive method for monitoring the drying process of glutinous rice using an HSI system coupled with chemometrics. This method can be aptly applied for the rapid detection and control of the drying process to ensure appropriate drying and effectively reduce grain loss due to over-drying.

#### 2. Materials and methods

#### 2.1. Sample collection and preparation

Fresh glutinous rice (paddy) was supplied by Berkat Padi Sdn Bhd, a local rice supplier in Malaysia. The collected rice was cleaned using paddy cleaner to remove unwanted particles such as immature grains, broken grains, stalk fragments, and foreign objects. The cleaned grains were sealed in an airtight plastic container and stored in a freezer (ACSON, ACF 30F(T), Malaysia) at a temperature of  $-5\,^{\circ}\text{C}$ . Before the experimentation, the initial MC of the grains was measured in triplicate using the standard oven drying method, and the resulting value was  $23.65\pm0.34$  %wb.

#### 2.2. Drying process of glutinous rice

The drying process of the glutinous rice was carried out using a hot air box dryer (Model 3021, Malaysia). The dryer has an external dimension of 650  $\times$  900  $\times$  1900 and an internal dimension of 0.59  $\times$  $0.58 \times 1.40$  m. The heat is externally produced by 2.5 kW and distributed by the blower into the drying chamber through perforated media. Before the drying commences, the fresh glutinous rice sample was withdrawn from the freezer and allowed to equilibrate with the ambient temperature. The dryer was powered for about 60 min to ensure the heat was evenly distributed in the drying chamber before loading the glutinous rice. Under the different temperatures (50  $^{\circ}\text{C}$  , 60  $^{\circ}\text{C}$  and 70  $^{\circ}\text{C}$  ) and grain layer thicknesses of 15 mm (120 g), 25 mm (190 g), 35 mm (280 g), and 45 mm (380 g), the glutinous rice was dried in three replicates which gave a total of 36 experimental runs. During the drying process, 10 g of the sample was collected at intervals of 30 min until the grains attained the critical moisture content (12 %), which denoted the level at which no spoilage could occur in the grains (Nath et al., 2022). A total of 178 samples were collected and used for the hyperspectral image acquisition, MC measurement, and appearance indices determination.

#### 2.2.1. Moisture measurements

The MC measurement was carried out using the oven-drying method. Five grams of the collected sample were placed in a laboratory oven (Carbolite, PF60, England) under  $105\,^{\circ}$ C for 24 h, and the electronic weighing balance was used to measure the weight before and after the drying. The MC of the sample was calculated using Eq. (1) (Qiao et al., 2022).

$$MC = \frac{m_b - m_a}{m_b} \times 100 \tag{1}$$

Where  $m_b$  is the mass of the sample before drying (g),  $m_a$  is the mass of the sample after drying (g).

# 2.2.2. Appearance indices measurement

Aside from the MC which is the commonly used quality metric for assessing the effectiveness of a grain drying process, the grain appearance is another important metric for assessing the drying process of food material. The change in colour and the golden index (GI) were selected as the appearance indices for the glutinous rice during the drying process. The standard CIEL\*a\*b\* colour channels of each sample were measured using a digital colourimeter (NR145, 3NH, Shenzhen, China). The instrument was initially calibrated using a standard white tab (D65) followed by the sample measurements. The colour change was calculated using Eq. (2)

$$\Delta E = \sqrt{\Delta L^{*2} + \Delta a^{*2} + \Delta b^{*2}} \tag{2}$$

where  $\Delta E$  is the colour change,  $\Delta L^*$  is the change in the lightness,  $\Delta a^*$  is the change in greenness/redness,  $\Delta b^*$  is the change in the blueness/yellowness.

The GI is a section in the yellow channel, and it was determined using a golden yellow index of the American standard test method (ASTM 313). The recorded L\*a\*b\* channel was transformed into an RGB channel using the built-in function of MATLAB 2023b The GI was calculated using Eq. (3)

$$GI = \frac{1 - B}{G} \tag{3}$$

where B is the blue channel and G is the green channel of the RGB standard.

# 2.3. Hyperspectral imaging setup and spectral acquisition

The hyperspectral images of the glutinous rice were acquired by using visible near-infrared hyperspectral (VNIR-HSI) set-up (Cubert,

# **Image acquisition set up** Computer ROI VNIR camera Camera Lamp Support Sample Movable 000000000000 platform Hypercube Spectra Reflectance Wavelength (nm)

Fig. 1. The setup of the visible-near infrared hyperspectral imaging system.

S185 FireflEYE, Germany). The spectral range of the VNIR-HIS ranged from 450 nm – 998 nm with a spectral sampling of 4 nm and  $1000 \times 1000$ pixels as the output spatial resolution. The schematic drawing for the setup of the VNIR-HSI system is shown in Fig. 1. The setup consists of a VNIR-HSI camera, a halogen lamp as the source of illumination, a fan to prevent overheating by cooling the system, a movable frame, and a computing system for acquisition controlling, image temporary storing, and processing of the hypercube image. The sampled glutinous rice was placed in a petri dish, and the hyperspectral images were collected sequentially. Prior to image acquisition the camera was calibrated using white and black reference images to reduce the effect of dark current and noise. The relationship between the raw and corrected image is expressed in Eq. (4). A rectangular area of 200×200 pixels with a high concentration of the grains and enough information to depict the glutinous rice sample was selected as the region of interest (ROI) of the image. Therefore, the average of the spectral data was obtained for each wavelength to represent the sample.

$$R = \frac{X - X_d}{X_w - X_d} \tag{4}$$

where *R* is the corrected image reflectance, *X* is the raw image sample,

 $X_w$  is the white reference image, and  $X_d$  is the dark reference image.

#### 2.4. Spectral preprocessing

Fig. 2 shows the flow chart for the steps involved in the data process and model development for monitoring the grain quality during the drying process using the HSI technique. The raw spectral data may vary differently due to light intensity, instrument noise, stray light, dark current, etc. It is necessary to reduce extraneous information that is irrelevant to the targeted properties of the sample through spectral preprocessing to improve the accuracy and prediction ability of the model (Panda et al., 2022; Tian et al., 2023). In this study, the obtained reflectance spectra from the HSI were subjected to 4 preprocessing methods that are commonly used for spectral data preprocessing in literature. This method includes moving window smoothing (MWS) with five window sizes, multiplicative scattering correction (MSC), Standard normal variate (SNV), and Savitzky-Golay first derivative (SG1D) with five window sizes. The raw spectral was used as a reference point for evaluating the effectiveness of the preprocessed method during the model development.

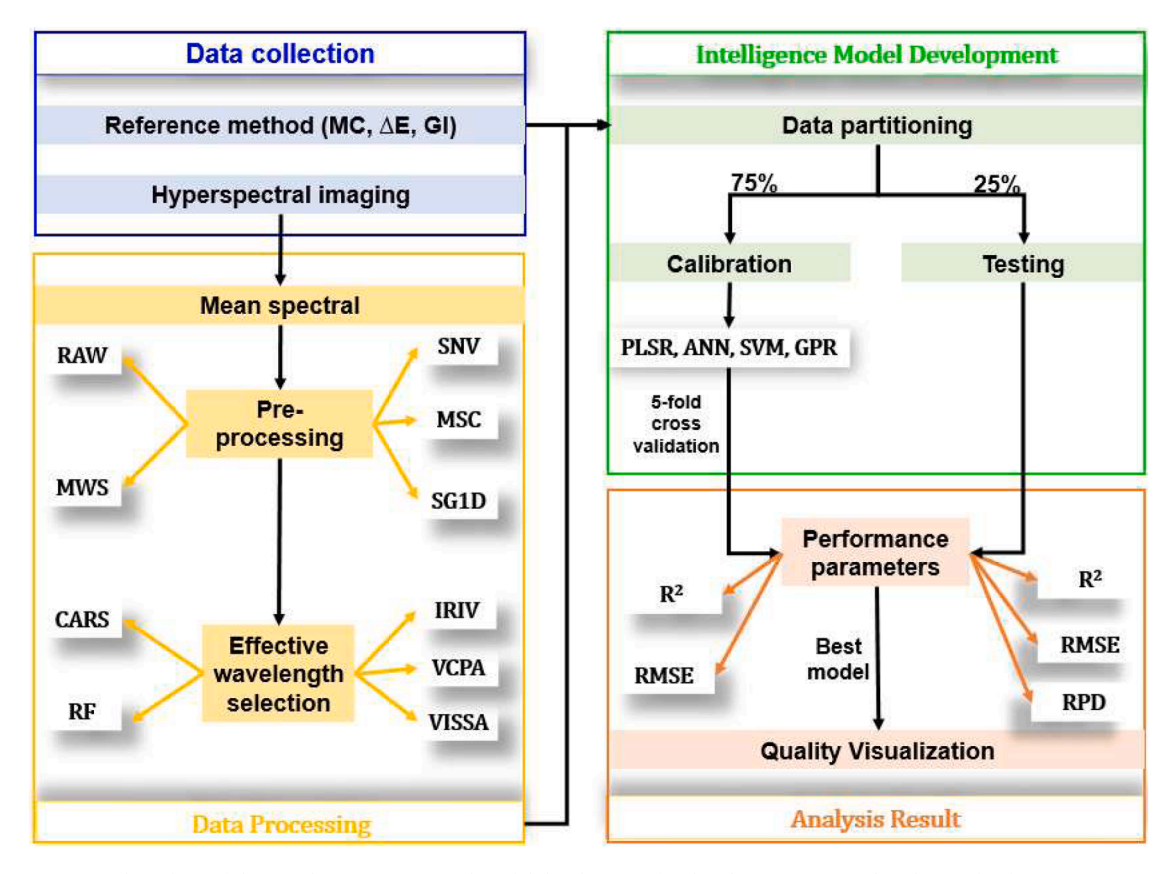


Fig. 2. Flow chart of the HSI data processing and model development for the glutinous rice quality during the drying process.

# 2.5. Effective wavelength selection

Hyperspectral image information exhibits characteristics such as multi-collinearity and high dimensionality with several redundant information that are laborious and time-consuming during processing (Song et al., 2023). The selection of the effective wavelength reduces the dimension of the full spectral feature. The wavelength selection offers a range of benefits by removing irrelevant and redundant information (Zhang et al., 2023a). Therefore, the processing time, execution speed, and accuracy in actualizing the real-time quality detections are enhanced (Song et al., 2023; Zheng et al., 2018). After selecting the most appropriate preprocessing method, the important wavelengths were selected using the variable iterative space shrinkage approach (VISSA), random frog (RF), variable combination population analysis (VCPA), Iteratively retains informative variables (IRIV), and Competitive adaptive reweighted sampling (CARS) (Jimoh & Hashim, 2024; Jimoh et al., 2025a).

#### 2.6. Model development

A total of 178 hyperspectral images were collected during the experiment and divided into the calibration and prediction data sets in a 3:1 ratio to develop the predictive model. The partitioning was done to ensure the produced model was accurate and effective. The Kennard-Stone method was used to divide the data. The method maximizes the Euclidean distance between the response to evenly cover the multi-dimensional space. Therefore, both partitions contains data with maximum variability of the original data (Zhang et al., 2023a). To maximize the accuracy of the quantitative model and avoid overfitting, 5-fold cross-validation method was employed during model training with calibration data set (Jimoh et al., 2025c, 2025a). The repeatability of the established quantitative models was demonstrated using prediction set samples excluding the response for testing the developed model

(Achata et al., 2021). The partial least square regression (PLSR) was used as the linear computational intelligence algorithm that was used for the model development, while artificial neural network (ANN) with multilayer perceptron, support vector machine (SVM), and Gaussian processes regression (GPR) were used as the nonlinear computational intelligence approach (Achata et al., 2021; Jimoh et al., 2024a).

## 2.6.1. Partial least square regression

The PLSR carries out the least squares approach by condensing data sets, comprising input and output variables, into several latent variables with the most significant amount of information. Therefore, the PLSR approach compensates for the principal component analysis limitations by considering the output variable for dimension reduction and satisfies Eq. (5) (Park et al., 2023; Xu et al., 2018). In this study, the PLSR model calibration was carried out with a mean center scaling, and the maximum latent variable was set to 10 with 5-fold cross-validation (Li et al., 2022).

$$Y = TP_t + EX = TQ_t + F (5)$$

where  $T = (t_1, t_2, ...., t_n)$  is the variable; E and F are random errors of Y and X, respectively.

## 2.6.2. Support vector machine

The SVM model converted the input data into a high-dimensional feature set using Kernel functions, including the linear, polynomial, and radial basis functions, to accurately predict the output parameter (Abdallah et al., 2022). SVM aims to find the hyperplane as a function of the input variable (Eq. (6)) and the best-predicted locations with minimal divergence from the response vector. To assure the fitness of the SVM technique, the method finds the ideal hyperplane function parameters with minimum residual (Eq. (7)) (Alaoui et al., 2023). In this study, the kernel function, penalty function, kernel scale, and box constraint were tunned using the Bayesian algorithm

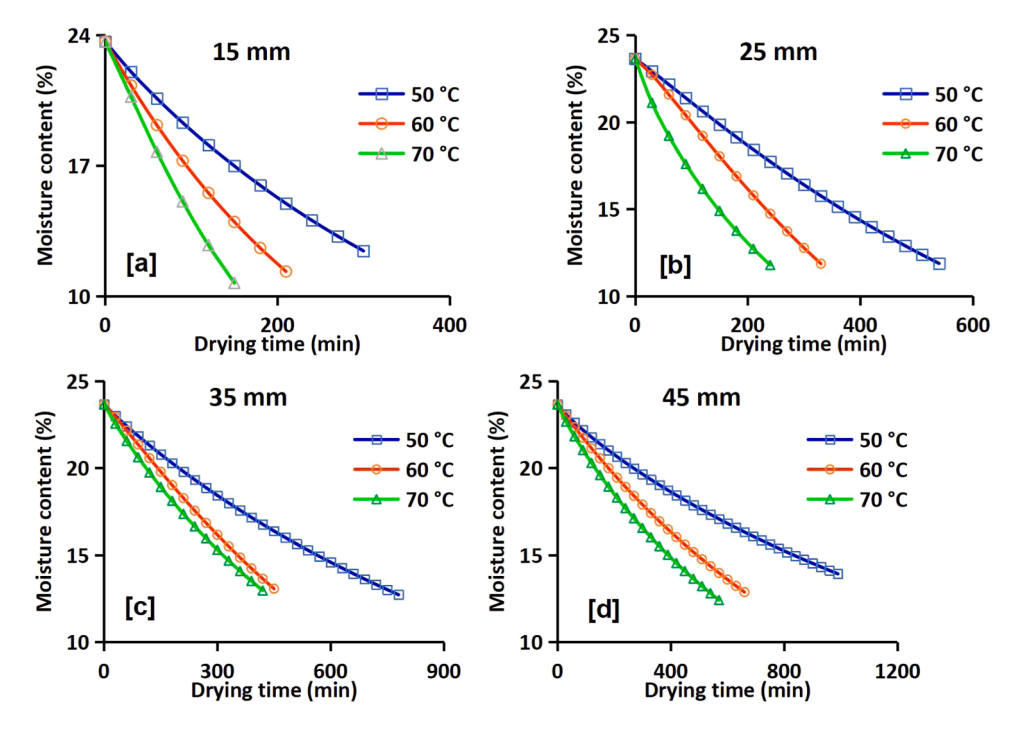


Fig. 3. Moisture content of glutinous rice against the time under different temperatures and layer thicknesses. [a]: 15 mm, [b]: 25 mm, [c]: 35 mm, and [d]: 45 mm.

$$f(x) = w, \emptyset(x) + b \tag{6}$$

$$(w^*.y^*) = \operatorname{argmin}_{w,b} \sum_{i=1}^{n} (y_i - (w, x_i) - b^2)$$
 (7)

where  $\emptyset$  (x) is the kernel function, and w and b are the hyperplane parameters of the model.

# 2.6.3. Gaussian process regression

GPR uses a kernel-based approach to represent the random variables in building the intelligent models. The data distribution curve for the GPR distribution is shaped similarly to the normal distribution curve (bell curve). Thus, the two fundamental parameters of the Gaussian distribution (the variance and the mean) can be used to explain the distribution. The relationship in Eq. (8) is used to compute the Gaussian process distribution (Jimoh et al., 2024a; Mohammadpour et al., 2022)

$$y \approx g_{\ell}(M(X), K(X, X'; \theta))$$
 (8)

where y is the model response, M(X) is the basis function, and K(X,X') is the kernel function.  $\theta$  is the set of other model hyperparameters, which includes sigma and scale values,

# 2.6.4. Artificial neural network

ANN is one of the widely adopted intelligence approaches to overcome the limitations of traditional statistical modelling methodologies, mainly when dealing with huge, noisy, and unstable data sets. The model was inspired by the behaviour of the human brain while resolving problems. The multilayer perceptron used for ANN model development in this study requires estimating the weight of the structure that connects the model neurons in the hidden layers (Park et al., 2023). The mean square error was used as the loss function, while the hyperparameters that were tuned to optimize the ANN model for effective prediction include the number of layers, transfer function, network optimizer, and learning rate.

# 2.7. Model accuracy indices

Evaluation of model accuracy is the most important aspect of model

development. The performance of the developed model during calibration they were computed and compared using the coefficient of determination of calibration ( $R_C^2$ ) and root mean squared error of calibration (RMSEC) shown in Eqs. (9) and 10, respectively. The coefficient of determination of prediction ( $R_p^2$ ), root mean squared error of prediction (RMSEP) and the mean absolute percentage deviation (MAPD) were computed for the prediction performance of the model using Eqs. (11), 12, and 13, respectively. The model with a higher  $R^2$  with lower RMSE and MAPD was considered the best model for predicting the moisture, change in colour, and golden index of glutinous rice (Guo et al., 2023b; Sun et al., 2019).

$$R_C^2 = 1 - \frac{\sum_{i=1}^{n} (Y_{C,i} - Y_i)^2}{\sum_{i=1}^{n} (Y_{C,i} - \overline{Y_i})^2}$$
(9)

$$RMSEC = \sqrt{\frac{\sum_{i=1}^{n} (Y_{C,i} - Y_i)^2}{n}}$$
 (10)

$$R_p^2 = 1 - \frac{\sum_{i=1}^n (Y_{P,i} - Y_i)^2}{\sum_{i=1}^n (Y_{P,i} - \overline{Y_i})^2}$$
(11)

$$RMSEP = \sqrt{\frac{\sum_{i=1}^{n} (Y_{P,i} - Y_i)^2}{n}}$$
 (12)

$$MAPD = \frac{1}{n} \sum_{i=1}^{n} \left[ \frac{|Y_{P,i} - Y_i|}{Y_{P,i}} \times 100 \right]$$
 (13)

where  $Y_{C,i}$  and  $Y_{P,i}$  are the modelled values for the calibration and prediction data set, respectively,  $Y_i$  and  $\overline{Y_i}$  are the reference and mean of experimental value, respectively, and n is the number of observations.

# 2.8. Glutinous rice quality visualization

The glutinous rice quality distribution during the drying process was visualized based on the approach outlined by Malegori et al. (2021). For HSI data, each pixel of the spatial information consists of a spectrum,

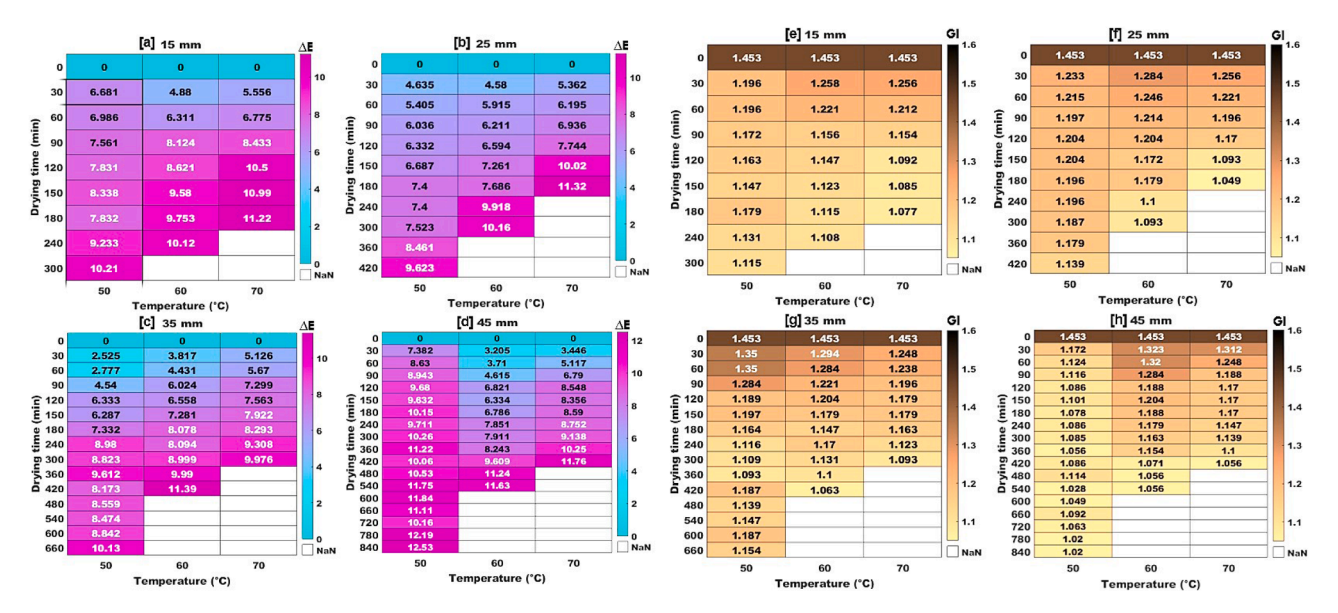


**Fig. 4.** Change in the colour ( $\Delta E$ ) and golden index (GI) of glutinous rice during the drying process for different temperatures and layer thicknesses: [a], [b], [c], and [d] denote the  $\Delta E$  under 15 mm, 25 mm, 35 mm, and 45 mm thicknesses respectively. [e], [f], [g], and [h] denote the GI under 15 mm, 25 mm, 35 mm and 45 mm thicknesses respectively.

and the selected best model was used for the determination of the corresponding grain quality in each pixel (Ahmed et al., 2024). In order to create chemical distribution map for the grain responses, The HSI was reshaped from a 3D to a 2D array with rows equal to the number of pixels in each wavelength and columns equal to the number of bands in the HSI data. The 2D array was subjected to the selected best preprocessing techniques followed by the effective wavelength selection techniques and the predictive model was used to determine the grain quality of each pixel which gave a 1D vector. Therefore, the 1D vector was reshaped into a 2D array with equal dimensions with the spatial resolution of the 3D HSI datacube. The distribution map of the grain qualities was visualised using a pseudocolour plot with linear scale to reshaped the 2D array (Jimoh et al., 2025a). All preprocess computation and effective wavelength selection and predictive model development and visualization of quality distribution map were computed using MATLAB 2023a software.

# 3. Result and discussion

# 3.1. Moisture content

The MC of glutinous rice against the drying time under different temperatures and layer thickness is shown in Fig. 3. The MC of the fresh glutinous rice reduces continuously with time throughout the drying process, regardless of temperature and layer thickness. The MC after 3 hours ranged between 8.89 % and 21.01 %, indicating variation in the moisture during the drying process and the influence of drying conditions on the rate of moisture removal from the glutinous rice. The speed of moisture removal increased with the increase in the temperature and decrease in the layer thickness. The lower moisture (8.89 %) after 3 hours was recorded at 70 °C and 15 mm, while the grain dried at the temperature of 50 °C and 45 mm thickness had the highest MC of 21.01 %. The effect of temperature and thickness in this study is consistent with the findings of Mondal et al. (2022), who found that temperature improves the diffusion of moisture by enhancing the heat and mass transfer between the grain and the heated environment of the drying system.

#### 3.2. Appearance indices

The continuous change in the colour and GI of glutinous rice samples during the drying process is shown in Figure 4(a-d) and Figure 4(e-h), respectively. The GI of the fresh glutinous rice was 1.453. The GI reduces continuously with the drying time while the  $\Delta E$  increases progressively. The GI ranged between 1.046 and 1.195 after 3 h of drying, while the  $\Delta E$ ranged between 6.79 and 11.32. The lowest  $\Delta E$  was obtained (1.046) under the temperature of 60 °C and thickness of 45 mm. The highest  $\Delta E$ (1.195) was obtained at the temperature of 70 °C and thickness of 25 mm. The highest GI (11.32) was obtained at a temperature of 50 °C and a thickness of 35 mm. The lowest GI (6.79) was obtained at a temperature of 70 C and a thickness of 25 mm. The progression shows that the  $\Delta E$ increases with the temperature and decreases with the layer thickness. In contrast, the GI increases with the layer thickness and decreases with the temperature. This outcome highlights the significant impact of drying conditions on the appearance of the grain throughout the drying process. Iheonye et al. (2019) suggest that dried grains exhibiting minimal appearance deviation from their fresh state are typically associated with higher nutrient retention and thus hold greater value. Consequently, grain processors and consumers generally prefer grains that experience minimal  $\Delta E$  and maintain a high GI (Fig. 4).

#### 3.3. Data outlier identification and removal

The Monte Carlo-partial least square technique was used to identify outliers in reflectance spectral information and response variables. The average and standard deviation were computed based on the root mean square error of cross-validation (RMSECV) of each sample. The standard deviation was plotted on the ordinate against the mean on the abscissa to visualise and identify the datum point, as shown in Fig. 5. The datum point of standard deviation was set to 2.0, 1.3, and 0.055 for the MC,  $\Delta E$  and GI, respectively. The limit for the mean values was set as 2.5 times the standard deviation limit, and the values above the set limit were identified as outliers. After the elimination of 11, 6, and 10 observations as outliers in MC,  $\Delta E$ , and GI, respectively, the  $R_C^2$  increased from 0.8493 to 0.9663 for the MC, 0.9307 to 0.9612 for  $\Delta E$ , and 0.93355 to 0.9557 for GI, which confirms the abnormalities of the eliminated values (Guo et al., 2023b).

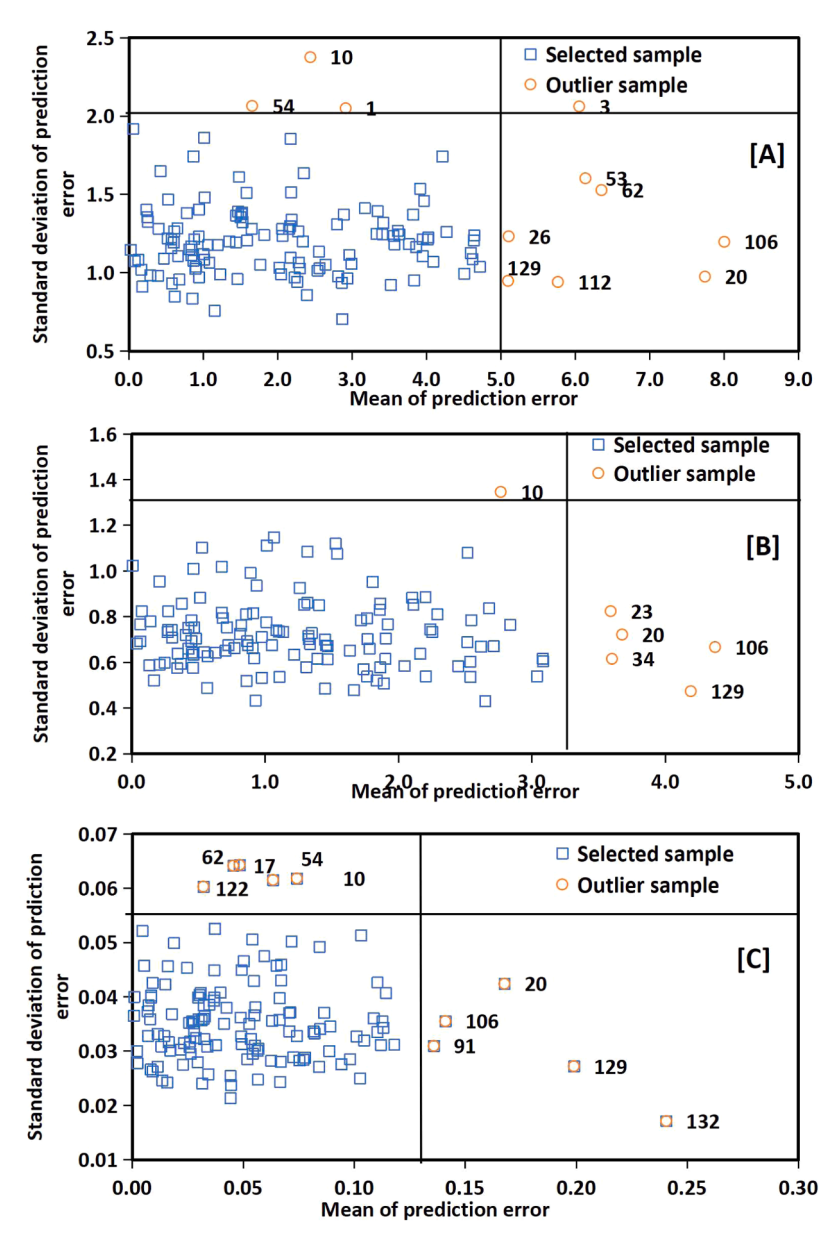


Fig. 5. Outlier detection using Monte Carlo sampling techniques. [A]: MC, [B]:  $\Delta E$ , and [C]: GI.

#### 3.4. Reflectance spectra characteristics

The HSI raw spectra range from 450 to 998 nm with 138 wavelength points and a sampling resolution of 4 nm is shown in Fig. 6a, it represents the average reflectance values for all pixels in the ROI of the samples. The reflectance from the least wavelength (450 nm) reduced continuously until 482 nm to 490 nm. Continuous increments follow this until the peak reflectance is attained at 900 nm with a slight absorbance valley between 730 nm and 750 nm for different samples, which is related to second overtone O—H and N—H stretches, and third overtone C—H (Jimoh et al., 2025a). The reflectance from 900 nm to 998 nm had a slight increment trend with another slight absorption valley between 920 nm and 950 nm, which was situated near the absorption valley of 960 nm, denoting second overtone O—H stretching and associated with grain moisture (Song et al., 2023).

#### 3.5. Spectra preprocessing method and model performance

Figure 6(b-e) depicts preprocessed spectral data from different processing methods, including MWS, MSC, SNV, and SG1D. The

preprocessing method reduced environmental, human, instrumental, and operational errors. MWS algorithms eliminate the noise and inconsistency in the spectral data. MSC technique reduces the multiplicative and additive error in the spectra. The SNV applies the normalisation method to minimise the multiplicative and additive effect in the spectra data. Using SG1D for the spectral data correction reduces particle offset and scattering effect at the spectral baseline. Models were developed for effective prediction of the reference quality index (MC, GI,  $\Delta E$ ) of glutinous rice during the drying process based on the full raw spectra and the preprocessing spectra. The model includes PLSR, SVM, GPR, and ANN algorithms. The performance accuracy of the preprocessing method with the model for effective determination of the reference quality of glutinous rice is summarised in Table A.1

# 3.5.1. Preprocessing and PLSR model performance

The calibration accuracy ( $R_C^2$ ) for RAW-PLSR model ranged from 95.57 % to 96.63 % with RMSEC ranging from 0.0256 to 0.9002 for the MC, GI and  $\Delta E$  of glutinous rice during drying. Testing RAW-PLSR model with prediction data set resulted in an accuracy span from 94.82 % to 95.99 % and the RMSEP were 1.0400, 0.6747, and 0.021 with MAPD of

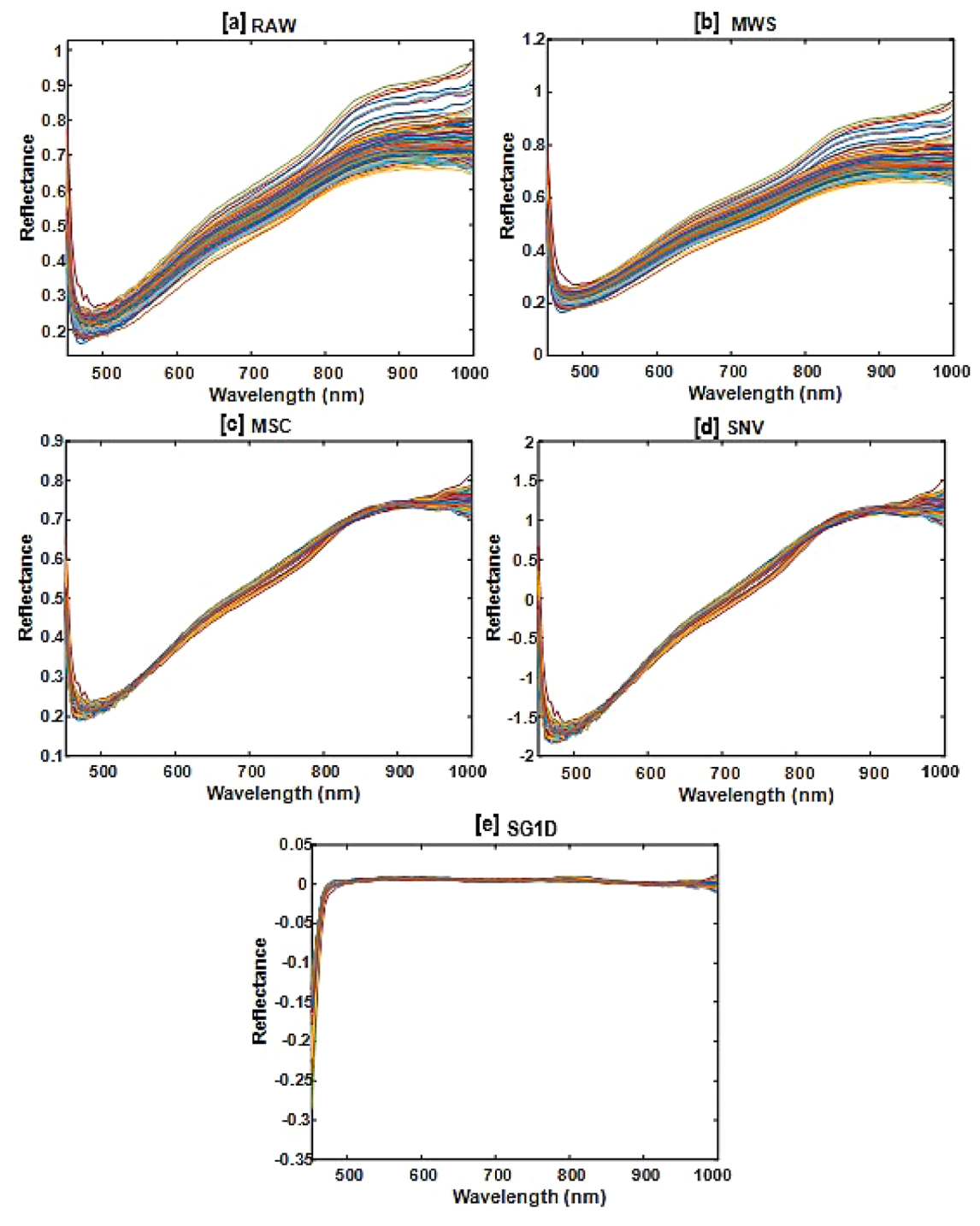


Fig. 6. Raw and preprocessed reflectance spectral data of glutinous rice: [a] RAW, [b] MWS, [c] MSC, [d] SNV, and [e] SG1D.

5.33 %, 7.15 %, and 1.84 % were obtained for the MC,  $\Delta E$  and GI respectively. SG1D-PLSR was adjudged with the best performance in predicting MC,  $\Delta E$  and GI of glutinous rice and increases the RAW-PLSR model accuracy. SG1D-PLSR model exhibits the most compelling performance compared to other preprocessing methods in predicting the quality of glutinous rice. The model had the highest  $R_C^2$ , and  $R_P^2$  values of 0.9800, and 0.9741, respectively, with the lowest RMSEC, RMSEP and MAPD of 0.6948, 0.8242 and 4.25 % for the moisture prediction. For  $\Delta E$ , the SG1D-PLSR model had the best performance. It has the highest  $R_C^2$  of 0.9751 and  $R_P^2$  of 0.9564 with the lowest RMSEC of 0.5166, RMSEP of 0.6169 and MAPD of 5.90 %. In the case of the GI of glutinous rice, the SG1D-PLSR model had the best performance with  $R_C^2$ , RMSEC,  $R_P^2$ ,

RMSEP and MAPD values of 0.9693, 0.0179, 0.9685, 0.0177 and 1.28 %, respectively (Table A1).

# 3.5.2. Preprocessing and SVM model performance

The calibration accuracy for RAW-SVM model ranged from 89.16 % to 100 % and RMSEC were 0.0675, 1.2606, and 0.0201 for the MC,  $\Delta$ E, and GI of glutinous rice during drying. By testing the RAW-SVM with the prediction data set, the results showed the  $R_P^2$  being equal to 0.9026, 0.8667, and 0.9558 and RMSEP of 1.5030, 1.0529, and 0.0253 with MAPD of 7.41 %, 15.01 %, and 1.59 % for the MC,  $\Delta$ E, and GI respectively. As compared to other preprocessing methods, the SG1D-SVM model had the best performance in the prediction of the MC,  $\Delta$ E, and

GI of glutinous rice measuring the drying process and it increases the model accuracy compared to RAW-SVM model. For MC prediction, the SG1D-SVM model had the highest degree of accuracy value ( $R_C^2=0.9986$ , and  $R_P^2=0.9881$ ) with relatively low residual index (RMSEC = 0.2428, RMSEP = 0.5925 and MAPD = 1.45 %). For the  $\Delta$ E, the model has the highest accuracy index ( $R_C^2=0.9772$  and  $R_P^2=0.9534$ ) with the lowest error index (RMSEC = 0.5525, RMSEP = 0.6013 and MAPD = 5.66 %). In the case of predicting the GI of the glutinous rice, the model had the highest accuracy index ( $R_C^2$  of 0.9969 and  $R_P^2$  of 0.9961) with the lowest residual index (RMSEC = 0.0074, RMSEP = 0.0072 and MAPD = 0.62 %) (Table A1).

#### 3.5.3. Preprocessing and GPR model performance

The accuracy of RAW - GPR model during calibration ranged from 90.41 % to 100 % and the RMSEC values were 0.0008, 1.2274, and 0.000016 for the MC,  $\Delta E$ , and GI, respectively. The result of testing the RAW-GPR model with new spectral data only (prediction data set) reveals that RAW-GPR model performance was  $R_p^2 = 0.8819$ , 0.8916, and 0.9999; RMSEP = 1.6564, 0.9612, and 0.000023 with MAPD of 8.05 %, 14.73 %, and 0.0017 % for the MC,  $\Delta E$ , and GI respectively. The SG1D-GPR model exhibits the best performance for the determination of MC and GI of glutinous rice. For the MC, the model had the highest  $R_c^2$ , and  $R_p^2$  values (1.0000 and 0.9999) with the lowest RMSEC, RMSEP, and MAPD values (0.000061, 0.000067, and 0.0036 %). For the GI, the model had high  $R_c^2$  and  $R_p^2$  values (1.0000, and 0.9999) with low RMSEC, RMSEP, and MAPD values (0.000017, 0.000016, and 0.0012 %). However, the SNV-GPR model exhibits the best performance with the highest degree of accuracy in prediction for the prediction of the  $\Delta E$ . The model had the highest  $R_c^2$  and  $R_p^2$  (1.0000 and 0.9999) with the lowest RMSEC, RMSEP, and MAPD values (0.000033, 0.000046, and 0.0051 %) (Table A.1).

# 3.5.4. Preprocessing and ANN model performance

The performance accuracy of the ANN model for the determination of the reference quality of glutinous rice is summarised in Table 4.4. The RAW-ANN model calibration had the  $R_C^2$  of 0.9996, 0.9016 and 0.9999 with RMSEC of 0.1143, 1.1640, and 0.0009 for the MC, ΔE and GI respectively. By using the RAW-ANN model for the prediction data set, the  $R_P^2$  of 0.9996, 0.8797 and 0.9999; RMSEP of 0.1068, 1.0072 and 0.0012 with MAPD of 0.57 %, 13.11 % and 0.07 % for the MC,  $\Delta E$  and GI were obtained respectively. Based on the comparison of the performance of all the preprocessing methods, the RAW-ANN model remains the best performance for predicting the MC of glutinous rice during the drying process. Whereas the SG1D-ANN model had the best performance for the prediction of the  $\Delta E$  and GI of glutinous rice during the drying process. For  $\Delta E$ , the model had the  $R_C^2$ , RMSEC,  $R_P^2$  RMSEP and MAPD values of 0.9673, 0.6750, 0.9053, 0.8086 and 5.77%, respectively. For GI, the  $R_C^2$ , RMSEC,  $R_P^2$  RMSEP and MAPD values were 0.9999, 0.0008, 0.9998, 0.0014, and 0.05 %, respectively. (Table A.1).

Generally, most of the preprocessing techniques in this study had shown a remarkable performance towards the effectiveness and accuracy of the developed model (calibration and prediction) for rapid determination of the MC,  $\Delta E$ , and GI of glutinous rice during the drying process. The RPD of all the models falls within the acceptable range (RPD > 1.5) for a reliable model except for the MWS-SVM, whose RPD = 1.39. According to He et al. (2023), the most appropriate preprocess technique should be chosen to assess the quality index and further processing effectively. Regarding the preprocessing techniques, the SG1D was adjudged as the best method for spectra preprocessing. Therefore, the SG1D was used for variable selection and new model development for rapid monitoring of the drying process of glutinous rice. Also, comparing the performance of all the developed models, SG1D-GPR, SNV-GPR, and SG1D-GPR were adjudged as the best models for predicting the MC,  $\Delta E$ , and GI of glutinous rice during the drying

process. Thus, linearity between the experimentally obtained quality of glutinous rice and predicted values as a function of full raw spectra, best preprocessing methods combined with linear (PLSR) and nonlinear (ANN, GPR, and SVM) computational intelligence for prediction of the MC,  $\Delta E$ , and GI of glutinous rice are presented in Figure A.1a to Figure A.1c respectively.

#### 3.6. Effective feature selection

#### 3.6.1. Competitive adaptive reweighted sampling

CARS algorithm with a predefined monte Carlos simulation of 50 iterations and 5-fold cross-validation for evaluating the model performance. The resulting variation in the progression of the RMSECV for different simulation runs is presented in Figure A2. The minimum RMSECV was obtained at the iteration index of 24, 25, and 14 for the MC,  $\Delta E$ , and GI index, respectively. The RMSEC value was 2.4520 for moisture, 1.5801 for  $\Delta E$ , and 0.0409 for GI. Under optimal number of runs from CARS algorithm, the selected wavelengths were 52 bands for MC, 49 bands for  $\Delta E$ , and 45 bands for GI. Therefore, selecting the effective wavelength resulted in a pronounced reduction of 66.67 %, 76.09 %, and 70.29 % of full wavelength for MC, and GI, respectively (Figure A2).

#### 3.6.2. Random frog

The RF algorithm's parameters were predefined as 1000 Monte Carlos simulations with an initial sampling of 2 minimum points while the variable index assessment was set as regression coefficients. The RMSEP of Monte Carlo simulation iterations for the RF algorithms is presented in Figure A3. The feature selection for the RF simulation was done at run with the lowest RMSEP, the values were 1.7567, 1.2492, and 0.0369 for the MC,  $\Delta E$ , and GI, respectively. The algorithm selects 35, 32, and 31 bands as the effective wavelength for the MC,  $\Delta E$ , and GI, which amount to 74.64 %, 76.81, and 77.54 % reduction in the full wavelength (Figure A3).

#### 3.6.3. Iteratively retains informative variables

The progression of variables retained by IRIV algorithm during the iteration rounds is presented in Figure A4a-c for MC,  $\Delta E$ , and GI of glutinous rice, respectively. The selected wavelength was reduced continuously until 54.35 %, 63.77 %, and 57.25 % of bands were in the first three rounds for the MC,  $\Delta E$ , and GI, respectively. Afterwards, the band removal rate became steady until the 12, 14, and 15 wavelengths were finally removed at the sixth iteration round through backward elimination. Therefore, compared to full wavelength, the selected wavelength covers 33.33 %, 23.91 %, and 29.71 % for MC, GI, and  $\Delta E$ , respectively (Figure A4).

# 3.6.4. Variable combination population analysis

The parameters of VCPA were set as follows: the exponentially decreasing function (EDF) runs were 50 times, the binary matrix sampling (BMS) runs were 1000 times, the selected wavelengths were determined by 5-fold cross-validation, and the ratio of the optimal subset was 0.1 (Zhang et al., 2023a). Figure A5 shows the variation in RMSECV during the EDF operation of VCPA algorithm for MC,  $\Delta E$  and GI of glutinous rice. RMSECV continuously reduces with the EDF runs. In feature selection, the least RMSECV was attained at the final runs and the values were 2.3462, 1.5880, and 0.0504 for the MC,  $\Delta E$ , and GI, respectively. Subsequently, 11, 13, and 13 bands were chosen as the effective wavelength for the MC,  $\Delta E$ , and GI, in order words, 92.03 %, 90.58 %, and 90.58 % of the full bands were removed as the redundant wavelength (Figure A5).

# 3.6.5. Variable iterative space shrinkage approach

Figure A6a-c shows the variation in the RMSECV obtained at different iteration numbers during computation with the VISSA algorithm. For the MC,  $\Delta E$ , and GI of the glutinous rice, a total of 25, 24, and

 Table 1

 Summary of computational intelligence model performance for MC under different effective wavelength selection techniques.

Parameter	Processing	Variable selection	$R_C^2$	RMSEC	$R_p^2$	RMSEP	MAPD (%)
MC	SG1D-PLSR	CARS	0.9579	1.0035	0.9501	1.1467	6.13
		RF	0.9488	1.1027	0.9476	1.1648	6.03
		IRIV	0.9379	1.2128	0.9116	1.5079	7.91
		VCPA	0.8025	2.1691	0.7799	2.1854	10.76
		VISSA	0.9508	1.0832	0.9336	1.3190	6.85
	SG1D-SVM	CARS	0.9588	1.0303	0.9582	1.0825	6.38
		RF	0.9748	0.7981	0.9662	1.0111	5.19
		IRIV	0.9581	1.0094	0.9505	1.1775	6.29
		VCPA	0.9938	0.3883	0.9932	0.4373	1.62
		VISSA	1.0000	0.0013	0.9999	0.0014	$7.36 \times 10^{-3}$
	SG1D-GPR	CARS	0.9573	1.0780	0.9563	1.0219	5.69
		RF	0.9079	1.5300	0.8887	1.7395	8.53
		IRIV	1.0000	0.0006	0.9999	0.0006	$2.95 \times 10^{-3}$
		VCPA	0.9353	1.4793	0.9086	1.7992	9.69
		VISSA	0.8692	1.7535	0.8679	1.8074	7.42
	SG1D-ANN	CARS	0.7989	2.1827	0.7889	2.1645	10.82
		RF	0.8025	2.1691	0.7799	2.1854	10.76
		IRIV	0.9823	0.6668	0.9641	0.9827	5.00
		VCPA	1.0000	0.0007	0.9999	0.0011	$5.52 \times 10^{-3}$
		VISSA	0.9505	1.0843	0.9317	1.3409	6.90

Table 2 Summary of computational intelligence model performance for  $\Delta E$  under different effective wavelength selection techniques.

Parameter	Processing	Variable selection	$R_C^2$	RMSEC	$R_p^2$	RMSEP	MAPD (%)
ΔΕ	SG1D-PLSR	CARS	0.9391	0.8338	0.9091	0.7808	7.58
		RF	0.9286	0.8834	0.8957	0.8413	7.56
		IRIV	0.9135	0.9600	0.8805	0.8895	8.06
		VCPA	0.7817	1.4967	0.6724	1.4327	14.01
		VISSA	0.9448	0.7866	0.8934	0.8480	9.02
	SG1D-SVM	CARS	0.9766	0.6235	0.9503	0.6521	4.09
		RF	0.8947	1.1103	0.8407	1.0141	8.40
		IRIV	0.9995	0.0808	0.9948	0.2624	0.98
		VCPA	0.7844	1.4953	0.6631	1.4457	14.22
		VISSA	0.8753	1.2688	0.8017	1.1761	11.79
	SG1D-GPR	CARS	0.9632	0.6956	0.9266	0.7297	6.77
		RF	0.9410	0.8367	0.9035	0.8133	7.35
		IRIV	0.9364	0.8623	0.8968	0.8367	7.39
		VCPA	1.0000	0.0004	0.9999	0.0003	3.15×10
		VISSA	0.9680	0.6386	0.9249	0.7269	7.49
	SG1D-ANN	CARS	0.9876	0.4997	0.9813	0.4890	4.05
		RF	0.9189	0.9710	0.8755	0.9158	8.65
		IRIV	0.9712	0.6022	0.9389	0.7087	5.41
		VCPA	0.7884	1.4883	0.6573	1.4655	14.66
		VISSA	0.9357	1.1162	0.8784	1.1727	11.95

 Table 3

 Summary of computational intelligence model performance for GI under different effective wavelength selection techniques.

Parameter	Processing	Variable selection	$R_C^2$	RMSEC	$R_p^2$	RMSEP	MAPD (%)
GI	SG1D-PLSR	CARS	0.9390	0.0253	0.8933	0.0333	2.31
		RF	0.9238	0.0287	0.9120	0.0302	2.03
		IRIV	0.9122	0.0291	0.9094	0.0301	2.05
		VCPA	0.7859	0.0441	0.7794	0.0459	3.15
		VISSA	0.9397	0.0246	0.9348	0.0258	1.62
	SG1D-SVM	CARS	0.9945	0.0093	0.9863	0.0124	0.80
		RF	0.9887	0.0123	0.9871	0.0124	0.80
		IRIV	0.9958	0.0080	0.9949	0.0074	0.61
		VCPA	0.9345	0.0268	0.9150	0.0318	1.65
		VISSA	0.9963	0.0077	0.9938	0.0085	0.71
	SG1D-GPR	CARS	1.0000	0.0000	0.9999	0.0000	$1.25 \times 10^{-3}$
		RF	1.0000	0.0000	0.9999	0.0000	$1.15 \times 10^{-3}$
		IRIV	1.0000	0.0000	0.9999	0.0000	$1.21 \times 10^{-3}$
		VCPA	0.9904	0.0129	0.9897	0.0126	0.90
		VISSA	1.0000	0.0000	1.0000	0.0000	$1.18 \times 10^{-3}$
	SG1D-ANN	CARS	0.9992	0.0029	0.9986	0.0040	0.07
		RF	0.9999	0.0007	0.9999	0.0011	0.05
		IRIV	0.9999	0.0009	0.9998	0.0013	0.06
		VCPA	0.9999	0.0010	0.9999	0.0011	0.05
		VISSA	0.9999	0.0009	0.9999	0.0012	0.05

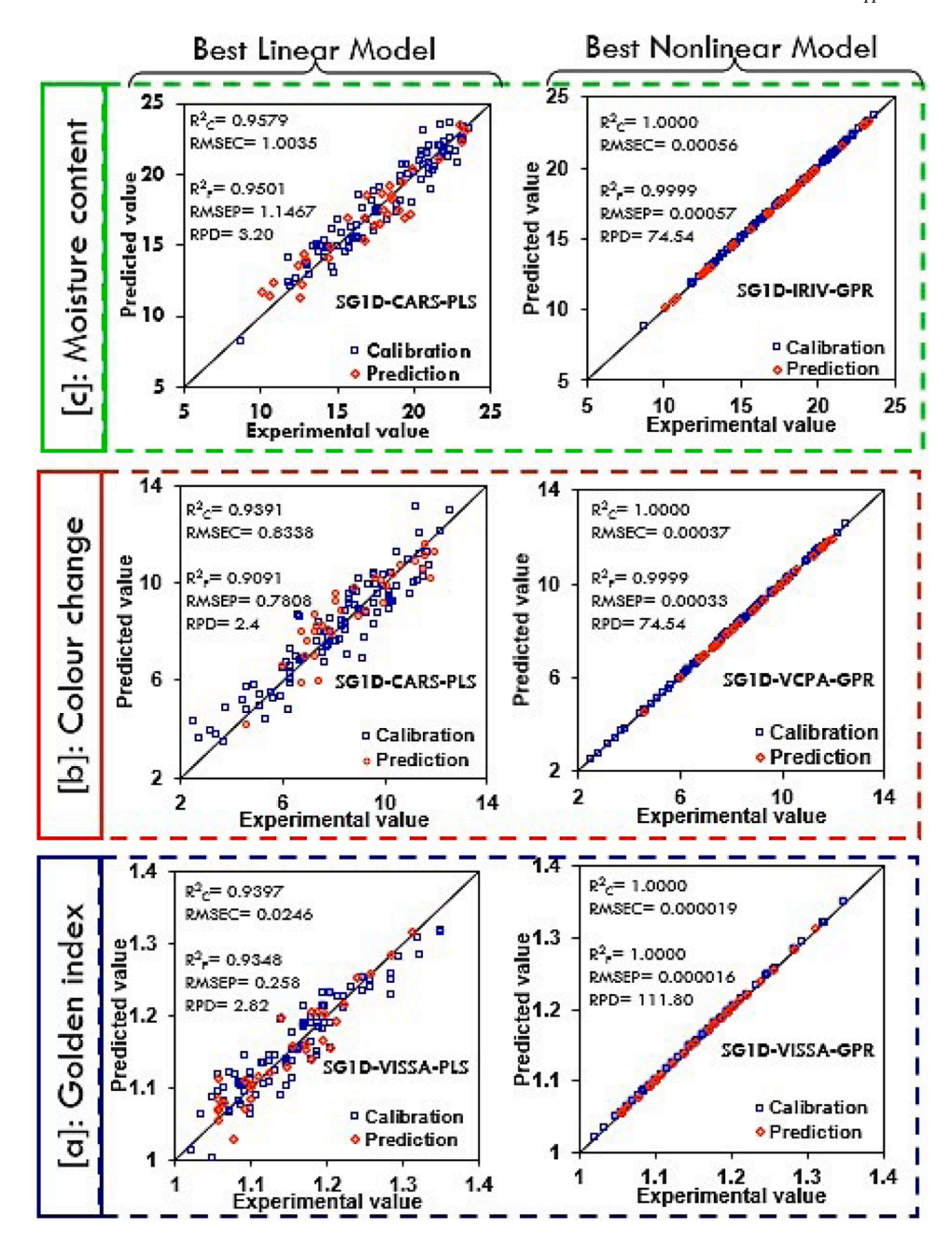


Fig. 7. The linear relationship between the experimentally obtained value and the predicted value of the best processing sequence for the PLSR model and the overall best model.

20 iterations were conducted, and they attained the minimum RMSECV value of 1.6936, 1.1094, and 0.0362, respectively. Figure A6d-f depicts the bands selected by the VISSA algorithm at final iteration rounds of 25, 24, and 20 for the MC,  $\Delta E$ , and GI of glutinous rice, respectively. The total selected wavelengths were 51, 52, and 47 bands for MC,  $\Delta E$ , and GI, which depict 63.04 %, 62.32 %, and 65.94 % reduction in the full wavelengths, respectively (Figure A6d-f).

# 3.7. Comparison of model accuracy

By using the selected best preprocessing method (SG1D), Table 1–Table 3 summarises the comparison result of the models developed as a function of selected effective wavelength from different techniques for MC,  $\Delta E$  and GI respectively. The linearity between experimental data and forecasted data from the best processing sequence with linear and nonlinear computational models is presented

in Fig. 7. In terms of linear computational intelligence (PLSR model), the SG1D preprocessing combined with CARS for selecting the effective bands (SG1D-CARS-PLSR) was adjudged as the best sequence for the determination of MC (Table 1) and  $\Delta E$  (Table 2) based on HSI data. For MC, the model had the highest  $R_{C}^{2}$  of 0.9579 and  $R_{p}^{2}$  of 0.9501, of with the lowest values of 1.0035, 1.1467 and 6.13 % for RMSEC, RMSEP and MAPD, respectively. For the  $\Delta E$ , the model had the highest  $R_{C}^{2}$  of 0.9391 and  $R_{p}^{2}$  of 0.9091, with the lowest values of RMSEC, RMSEP and MAPD of 0.8338, 0.7808 and 7.58 % respectively. However, SG1D-VISSA-PLSR had the best prediction performance for the GI as shown in Table 3. The model had the highest  $R_{C}^{2}$  of 0.9397 and  $R_{p}^{2}$  of 0.9348, with the lowest values of RMSEC, RMSEP and MAPD of 0.0246, 0.0258 and 1.62 % respectively (Fig. 7). Similar to the findings of this study, Song et al. (2023) obtained an accuracy of  $R_{p}^{2}=0.9643$ , with RMSEP of 0.0032 with RPD of 5.38 for predicting the moisture content of rice using HSI

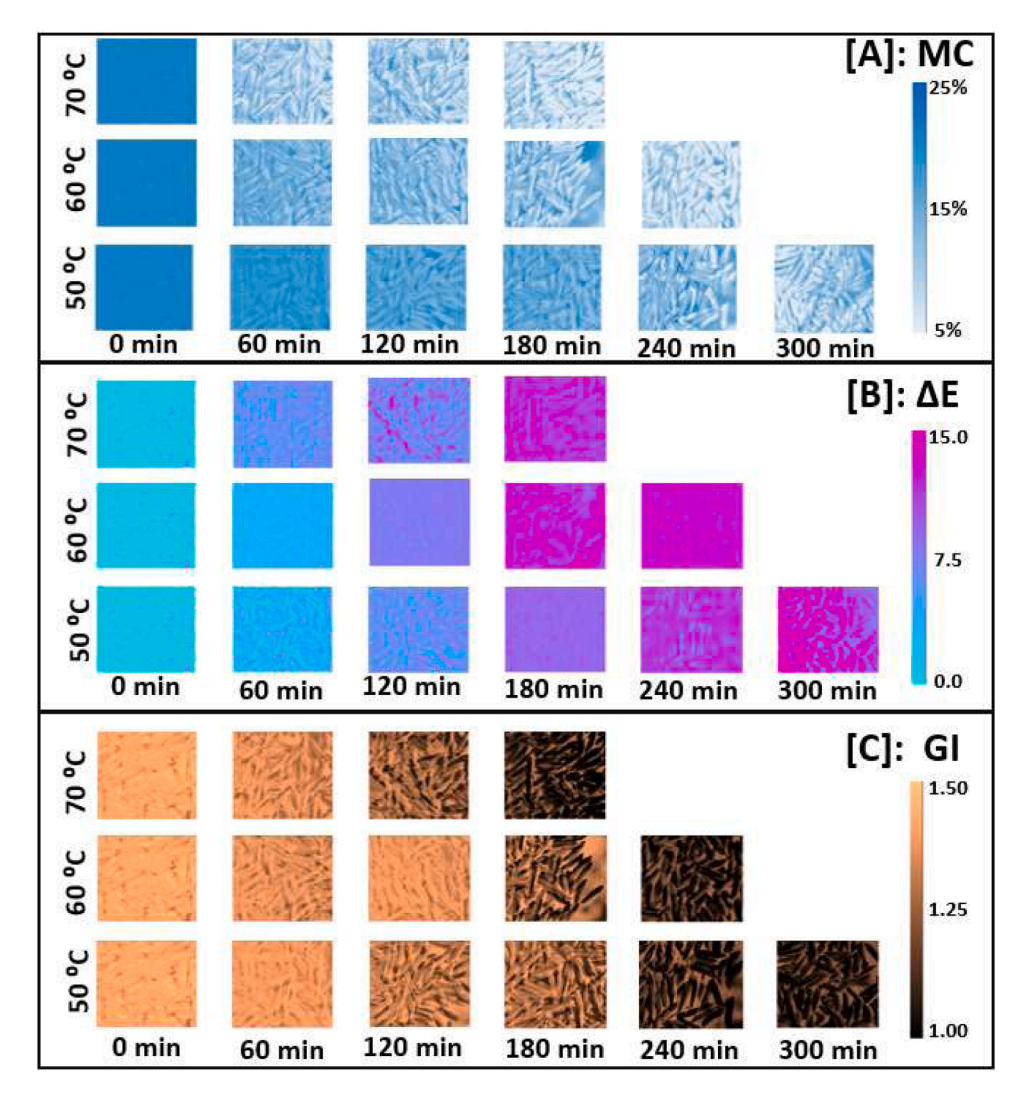


Fig. 8. Glutinous rice quality distribution during the drying process.

coupled with CARS-PLSR. Guo et al. (2023b) determine the MC of soybean seed using a visible near-infrared HSI system and obtain an accuracy of  $R_p^2$  of 0.9713, RMSEP of 0.307 and RPD of 6.058 using PLSR model couples with visa-SPA for the effective wavelength selection. Sun et al. (2019) recorded an accuracy of 0.9363, 0.7021, and 3.99 for  $R_p^2$ , RMSEP and RPD, respectively, in predicting peanut moisture using HSI combined with SPA-PLSR model. Zhang et al. (2023a) determined the MC of wheat flour using near-infrared HSI (969–2173 nm). The developed VCPA-PLSR model attained an accuracy of 0.6960, 0.3362, and 2.1.83 for  $R_p^2$ , RMSEP and RPD respectively. Whereas the IRIV-PLSR gave an accuracy of 0.8146, 0.2625 and 2.34 for  $R_p^2$ , RMSEP and RPD respectively.

In nonlinear computational intelligence model (ANN, GPR, and SVM), the SG1D-IRIV-GPR had the overall best performance in MC prediction. The model had the highest accuracy index ( $R_C^2$  of 1.0000 and  $R_p^2$  of 0.9999,) with the lowest error index (RMSEC, RMSEP and MAPD of 0.00056, 0.00057 and 0.0029 % respectively). For the  $\Delta$ E, The SG1D-VCPA- GPR had the best prediction performance. The model had the highest accuracy  $R_C^2$  of 1.0000 and  $R_p^2$  of 0.9999, with the lowest values of RMSEC, RMSEP and MAPD of 0.00037, 0.00033 and 0.0031 %, respectively. The SG1D-VISSA-GPR had the overall best performance for the prediction of the GI. The model had the highest accuracy index ( $R_C^2$  of 1.0000 and  $R_p^2$  of 1.0000) with the lowest residual index where the RMSEC, RMSEP and MAPD are 0.000019, 0.000016 and 0.0012 %,

respectively (Fig. 7).

#### 3.8. Spatial visualization of the grain quality

The reliability and accuracy of the developed HSI-based model can be conveyed by plotting the distribution maps for the targeted properties using the HSI data. In cases where the interpretation of the distribution map and its consequences are incorrectly represented, the developed model is considered inaccurate. Consequently, the deployment of the models is not advisable and recalibration of the model is essential (Ahmed et al., 2024). Therefore, the distribution map of the glutinous rice quality offers additional information in affirming the accuracy of the prediction model. Fig. 8 shows the progression in the MC,  $\Delta E$ , and GI during the drying process under different temperatures for 15 mm thickness. The figure reconstructs the properties obtained from best predictive model as a function of the selected effective wavelength. Therefore, the resulting map effectively represents the distribution of MC, ΔE, and GI of glutinous rice during the drying process. Fig. 8a-c presents the relative distribution of MC,  $\Delta E$ , and GI, respectively, with a linear colour scale for mapping each quality and ensures that similar predicted values were assigned with comparable colour properties. The grain quality distribution map does not only depict the quality distribution at pixel level but also presents the potential of HSI in visualizing the pixel-wise quality of glutinous rice which might be difficult to distinguish by unaided human eye. Consequently, the development of a

visual map for the spatial distribution of the grain quality parameters is essential in the application of HSI for monitoring the drying process of grain.

#### 4. Conclusion

This study evaluates the use of a visible-near infrared HSI system for monitoring the drying process of glutinous rice. The MC,  $\Delta E$ , and GI of the glutinous rice were predicted by harnessing the functionality of the HSI system when coupled with different preprocessing methods and effective wavelength selection techniques. The spectral data was preprocessed using four different methods (MWS, SNV, MSC, and SG1D), and the raw spectra were used as the reference point for comparison. CARS, RF, IRIV, VCPA, and VISSA algorithms were used to select effective wavelengths. PLSR, ANN, SVM, and GPR were developed for the prediction of MC,  $\Delta E$ , and GI of the glutinous rice. The result shows that the SG1D technique is the most effective method for spectral preprocessing because of its higher accuracy in predicting the MC,  $\Delta E$ , and GI of glutinous rice (0.9564  $\le R_P^2 \le 0.9741$ , 0.0177  $\le RMSEP \le 0.8242$ and  $1.28 \le MAPD \le 5.90$  for PLSR model). By using the PLSR model, the CARS-SG1D-PLSR gave the best performance for the MC and  $\Delta E$  of glutinous rice. The model has a higher  $R_p^2$  of 0.9501, RMSEP of 1.1467 and MAPD of 6.13 % for MC, with  $R_p^2$  of 0.9091, RMSEP of 0.7808, and MAPD of 7.58 % for  $\Delta E$ . VISSA-SG1D-PLSR model gave the best result for the determination of GI with  $R_p^2$  of 0.9348, RMSEP of 0.0258, and MAPD of 1.62 %. The comparison of all the models shows that the SG1D-IRIV-GPR, SGID-VCPA-GPR, and SGID-VISSA-GPR are the overall best models for perfect prediction ( $R_p^2 \ge 99.99$  %) of the MC,  $\Delta E$  and GI during the drying process. Therefore, processing sequences and models were recommended as a basis for developing intelligent devices for rapid detection, monitoring, and controlling the drying process of glutinous rice in the grain processing industry.

#### CRediT authorship contribution statement

Kabiru Ayobami Jimoh: Validation, Methodology, Investigation, Formal analysis, Data curation. Norhashila Hashim: Writing – review & editing, Supervision, Resources, Project administration, Conceptualization. Rosnah Shamsudin: Writing – review & editing, Supervision. Hasfalina Che Man: Writing – review & editing, Supervision. Mahirah Jahari: Writing – review & editing, Supervision.

# Declaration of competing interest

The authors declare that they have no known competing financial interests or personal relationships that could have appeared to influence the work reported in this paper.

#### Acknowledgments

The authors acknowledge the financial support of the Ministry of Higher Education, Malaysia, through the Transdisciplinary Research Grant Scheme Project (TRGS/1/2020/UPM/02/7).

# Ethical statement

The study titled "Rapid and non-destructive monitoring of the drying process of glutinous rice using visible-near infrared hyperspectral imaging" did not involve any experiments on humans or animals. The research was solely focused on the drying process of glutinous rice and utilized non-destructive imaging techniques. Therefore, no ethical approval was required for human or animal studies.

All procedures and methodologies adhered to ethical research practices, and the study was conducted in compliance with the guide-lines and standards of scientific integrity.

#### Supplementary materials

Supplementary material associated with this article can be found, in the online version, at doi:10.1016/j.afres.2025.100955.

#### Data availability

Data will be made available on request.

#### References

- Abdallah, M., Mohammadi, B., Modathir, M. A., Omer, A., Cheraghalizadeh, M., Eldow, M. E. E., & Duan, Z. (2022). Reference evapotranspiration estimation in hyper-arid regions via p-vine copula based-quantile regression and comparison with empirical approaches and machine learning models. *Journal of Hydrology: Regional Studies*, 44, Article 101259. https://doi.org/10.1016/j.ejrh.2022.101259
- Achata, E. M., Esquerre, C., Ojha, K. S., Tiwari, B. K., & O'Donnell, C. P. (2021). Development of NIR-HSI and chemometrics process analytical technology for drying of beef jerky. *Innovative Food Science and Emerging Technologies*, 69, Article 102611. https://doi.org/10.1016/j.ifset.2021.102611
- Ahmed, T., Wijewardane, N. K., Lu, Y., Jones, D. S., Kudenov, M., Williams, C., Villordon, A., & Kamruzzaman, M. (2024). Advancing sweetpotato quality assessment with hyperspectral imaging and explainable artificial intelligence. Computers and Electronics in Agriculture, 220(January), Article 108855. https://doi.org/10.1016/j.compag.2024.108855
- Alaoui, M. E., Chahidi, L. O., Rougui, M., Mechaqrane, A., & Allal, S. (2023). Evaluation of CFD and machine learning methods on predicting greenhouse microclimate parameters with the assessment of seasonality impact on machine learning perfomance. Scientific African, 19, Article e01578. https://doi.org/10.1016/j. sciaf.2023.e01578
- Guo, Z., Zhang, J., Dong, H., Sun, J., Huang, J., Li, S., Ma, C., Guo, Y., & Sun, X. (2023a). Spatio-temporal distribution patterns and quantitative detection of aflatoxin B1 and total aflatoxin in peanut kernels explored by short-wave infrared hyperspectral imaging. Food Chemistry, 424(266), Article 136441. https://doi.org/10.1016/j.foodchem.2023.136441
- Guo, Z., Zhang, J., Ma, C., Yin, X., Guo, Y., Sun, X., & Jin, C. (2023b). Application of visible-near-infrared hyperspectral imaging technology coupled with wavelength selection algorithm for rapid determination of moisture content of soybean seeds. *Journal of Food Composition and Analysis*, 116(June 2022), Article 105048. https:// doi.org/10.1016/j.jfca.2022.105048
- He, H. J., Wang, Y., Ou, X., Ma, H., Liu, H., & Yan, J. (2023). Rapid determination of chemical compositions in chicken flesh by mining hyperspectral data. *Journal of Food Composition and Analysis*, 116(September 2022), Article 105069. https://doi.org/ 10.1016/j.ifca.2022.105069
- Huang, H., Fei, X., Hu, X., Tian, J., Ju, J., Luo, H., & Huang, D. (2023). Analysis of the spectral and textural features of hyperspectral images for the nondestructive prediction of amylopectin and amylose contents of sorghum. *Journal of Food Composition and Analysis*, 115, Article 105018. https://doi.org/10.1016/j. ifca.2022.105018
- Huang, H., Hu, X., Tian, J., Jiang, X., Sun, T., Luo, H., & Huang, D. (2021). Rapid and nondestructive prediction of amylose and amylopectin contents in sorghum based on hyperspectral imaging. Food Chemistry, 359, Article 129954. https://doi.org/ 10.1016/j.foodchem.2021.129954
- Iheonye, A., Gariepy, Y., & Raghavan, V. (2019). Computer vision for real-time monitoring of shrinkage for peas dried in a fluidized bed dryer. *Drying Technology*, 38 (1–2), 130–146. https://doi.org/10.1080/07373937.2019.1649277
- Jimoh, K. A., & Hashim, N. (2024). Recent advances in non-invasive techniques for assessing food quality: Applications and innovations. Advances in food and nutrition research. Elsevier. https://doi.org/10.1016/bs.afnr.2024.09.006
- Jimoh, K. A., Hashim, N., Shamsudin, R., Che, H., & Jahari, M. (2025b). Assessment of performance and quality indices of glutinous rice under different drying methods. Sustainable Energy Technologies and Assessments, 73, Article 104161. https://doi.org/ 10.1016/j.seta.2024.104161
- Jimoh, K. A., Hashim, N., Shamsudin, R., Che, H., Jahari, M., & Eka, R. (2024b). Understanding the evolution of moisture during isothermal dehydration of glutinous rice through global sensitivity analysis. *Innovative Food Science and Emerging Technologies*, 95, Article 103733. https://doi.org/10.1016/j.ifset.2024.103733
- Jimoh, K. A., Hashim, N., Shamsudin, R., Che, H., Jahari, M., Nurain, P., Ahmad, M., & Onwude, D. I. (2025a). Hyperspectral imaging for detection of macronutrients retained in glutinous rice under different drying conditions. *Current Research in Food Science*, 10, Article 100963. https://doi.org/10.1016/j.crfs.2024.100963
- Jimoh, K. A., Hashim, N., Shamsudin, R., Che Man, H., & Jahari, M. (2025c). Development of near-infrared hyperspectral-based smart interface for glutinous rice quality detection. Food Control, 174(February), Article 111252. https://doi.org/ 10.1016/j.foodcont.2025.111252
- Jimoh, K. A., Hashim, N., Shamsudin, R., Man, H. C., & Jahari, M. (2023b). Recent advances of optical imaging in the drying process of grains – A review. *Journal of Stored Products Research*, 103, Article 102145. https://doi.org/10.1016/j. isnr.2023.102145
- Jimoh, K. A., Hashim, N., Shamsudin, R., Man, H. C., & Jahari, M. (2024a). Optimization of computational intelligence approach for the prediction of glutinous rice dehydration. *Journal of the Science of Food and Agriculture*. https://doi.org/10.1002/ jsfa.13445

- Jimoh, K. A., Hashim, N., Shamsudin, R., Man, H. C., Jahari, M., & Onwude, D. I. (2023a). Recent advances in the drying process of grains. Food Engineering Reviews. https://doi.org/10.1007/s12393-023-09333-7
- Kiani, S., Minaei, S., & Ghasemi-Varnamkhasti, M. (2018). Real-time aroma monitoring of mint (Mentha spicata L.) leaves during the drying process using electronic nose system. Measurement: Journal of the International Measurement Confederation, 124, 447–452. https://doi.org/10.1016/j.measurement.2018.03.033
- Li, Y., Ding, G., Yokoyama, W., & Zhong, F. (2018). Characteristics of annealed glutinous rice flour and its formation of fast-frozen dumplings. *Journal of Cereal Science*, 79, 106–112. https://doi.org/10.1016/j.jcs.2017.09.016
- Li, Y., Ma, B., Li, C., & Yu, G. (2022). Accurate prediction of soluble solid content in dried hami jujube using SWIR hyperspectral imaging with comparative analysis of models. *Computers and Electronics in Agriculture*, 193(December 2021), Article 106655. https://doi.org/10.1016/j.compag.2021.106655
- Malegori, C., Oliveri, P., Mustorgi, E., Boggiani, M. A., Pastorini, G., & Casale, M. (2021).
  An in-depth study of cheese ripening by means of NIR hyperspectral imaging: Spatial mapping of dehydration, proteolysis and lipolysis. Food Chemistry, 343(November 2020), Article 128547. https://doi.org/10.1016/j.foodchem.2020.128547
- Mohammadpour, J., Husain, S., Salehi, F., & Lee, A. (2022). Machine learning regression-CFD models for the nanofluid heat transfer of a microchannel heat sink with double synthetic jets. *International Communications in Heat and Mass Transfer, 130*, Article 105808. https://doi.org/10.1016/j.icheatmasstransfer.2021.105808
- Mondal, M. H. T., Akhtaruzzaman, M., & Sarker, M. S. H. (2022). Modeling of dehydration and color degradation kinetics of maize grain for mixed flow dryer. *Journal of Agriculture and Food Research*, 9(October 2021), Article 100359. https://doi.org/10.1016/j.jafr.2022.100359
- Nath, S., Bhattacharjee, P., Bhattacharjee, S., Datta, J., & Dolai, A. K. (2022). Grain characteristics, proximate composition, phytochemical capacity, and mineral content of selected aromatic and non-aromatic rice accessions commonly cultivated in the North-East indian plain belt. Applied Food Research, 2(1), Article 100067. https://doi.org/10.1016/j.afres.2022.100067
- Panda, B. K., Mishra, G., Ramirez, W. A., Jung, H., Singh, C. B., Lee, S. H., & Lee, I. (2022). Rancidity and moisture estimation in shelled almond kernels using NIR hyperspectral imaging and chemometric analysis. *Journal of Food Engineering*, 318, Article 110889. https://doi.org/10.1016/j.jfoodeng.2021.110889
- Park, S., Yang, M., Yim, D. G., Jo, C., & Kim, G. (2023). VIS/NIR hyperspectral imaging with artificial neural networks to evaluate the content of thiobarbituric acid reactive substances in beef muscle. *Journal of Food Engineering*, 350(September 2022), Article 111500. https://doi.org/10.1016/j.ifoodeng.2023.111500
- Qiao, M., Xu, Y., Xia, G., Su, Y., Lu, B., Gao, X., & Fan, H. (2022). Determination of hardness for maize kernels based on hyperspectral imaging. Food Chemistry, 366 (March 2021). Article 130559. https://doi.org/10.1016/j.foodchem.2021.130559
- Qiu, S., Abbaspourrad, A., & Padilla-Zakour, O. I. (2021). Changes in the glutinous rice grain and physicochemical properties of its starch upon moderate treatment with pulsed electric field. Foods, 10(2), 1–14. https://doi.org/10.3390/foods10020395
- Qiu, S., Punzalan, M. E., Abbaspourrad, A., & Padilla-Zakour, O. I. (2020). High water content, maltose and sodium dodecyl sulfate were effective in preventing the long-term retrogradation of glutinous rice grains A comparative study. Food Hydrocolloids, 98, Article 105247. https://doi.org/10.1016/j.foodhyd.2019.105247
   Ren, G., Ning, J., & Zhang, Z. (2020). Intelligent assessment of tea quality employing
- Ren, G., Ning, J., & Zhang, Z. (2020). Intelligent assessment of tea quality employing visible-near infrared spectra combined with a hybrid variable selection strategy. *Microchemical Journal*, 157, Article 105085. https://doi.org/10.1016/j. microc. 2020.105085
- Saha, D., Senthilkumar, T., Sharma, S., Singh, C. B., & Manickavasagan, A. (2023).
  Application of near-infrared hyperspectral imaging coupled with chemometrics for rapid and non-destructive prediction of protein content in single chickpea seed.

- Journal of Food Composition and Analysis, 115(June 2022), Article 104938. https://doi.org/10.1016/j.jfca.2022.104938
- Sharma, S., Sumesh, K. C., & Sirisomboon, P. (2022). Rapid ripening stage classification and dry matter prediction of durian pulp using a pushbroom near infrared hyperspectral imaging system. *Measurement: Journal of the International Measurement Confederation*, 189, Article 110464. https://doi.org/10.1016/j. measurement.2021.110464
- Shi, S., Pan, K., Yu, M., Li, L., Tang, J., Cheng, B., Liu, J., Cao, C., & Jiang, Y. (2022). Differences in starch multi-layer structure, pasting, and rice eating quality between fresh rice and 7 years stored rice. *Current Research in Food Science*, 5(August), 1379–1385. https://doi.org/10.1016/j.crfs.2022.08.013
- Song, Y., Cao, S., Chu, X., Zhou, Y., Xu, Y., Sun, T., Zhou, G., & Liu, X. (2023). Non-destructive detection of moisture and fatty acid content in rice using hyperspectral imaging and chemometrics. *Journal of Food Composition and Analysis*, 121(May), Article 105397. https://doi.org/10.1016/j.jfca.2023.105397
- Sun, J., Shi, X., Zhang, H., Xia, L., Guo, Y., & Sun, X. (2019). Detection of moisture content in peanut kernels using hyperspectral imaging technology coupled with chemometrics. *Journal of Food Process Engineering*, 42(7), 1–10. https://doi.org/ 10.1111/jfpe.13263
- Tao, F., Yao, H., Hruska, Z., Kincaid, R., & Rajasekaran, K. (2022). Near-infrared hyperspectral imaging for evaluation of aflatoxin contamination in corn kernels. *Biosystems Engineering*, 221, 181–194. https://doi.org/10.1016/j. biosystemseng. 2022. 07.002
- Tian, P., Meng, Q., Wu, Z., Lin, J., Huang, X., Zhu, H., Zhou, X., Qiu, Z., Huang, Y., & Li, Y. (2023). Detection of mango soluble solid content using hyperspectral imaging technology. *Infrared Physics and Technology*, 129. https://doi.org/10.1016/j.infrared.2023.104576
- Varela, J. I., Miller, N. D., Infante, V., Kaeppler, S. M., de Leon, N., & Spalding, E. P. (2022). A novel high-throughput hyperspectral scanner and analytical methods for predicting maize kernel composition and physical traits. *Food Chemistry*, 391 (December 2021), Article 133264. https://doi.org/10.1016/j.foodchem.2022.133264
- Xu, D., Ma, W., Chen, S., Jiang, Q., He, K., & Shi, Z. (2018). Assessment of important soil properties related to Chinese soil taxonomy based on vis–NIR reflectance spectroscopy. Computers and Electronics in Agriculture, 144, 1–8. https://doi.org/ 10.1016/i.compag.2017.11.029
- Zhang, J., Guo, Z., Ren, Z., Wang, S., Yue, M., Zhang, S., Yin, X., Gong, K., & Ma, C. (2023a). Rapid determination of protein, starch and moisture content in wheat flour by near-infrared hyperspectral imaging. *Journal of Food Composition and Analysis*, 117. Article 105134. https://doi.org/10.1016/j.ifca.2023.105134
- Zhang, L., Zhang, Q., Wu, J., Liu, Y., Yu, L., & Chen, Y. (2022). Moisture detection of single corn seed based on hyperspectral imaging and deep learning. *Infrared Physics* and Technology, 125(June). https://doi.org/10.1016/j.infrared.2022.104279
- Zhang, T., Lu, L., Yang, N., Fisk, I. D., Wei, W., Wang, L., Li, J., Sun, Q., & Zeng, R. (2023b). Integration of hyperspectral imaging, non-targeted metabolomics and machine learning for vigour prediction of naturally and accelerated aged sweetcorn seeds. *Food Control*, 153(January), Article 109930. https://doi.org/10.1016/j.foodcont.2023.109930
- Zheng, H., Cheng, T., Li, D., Yao, X., Tian, Y., Cao, W., & Zhu, Y. (2018). Combining unmanned aerial vehicle (UAV)-based multispectral imagery and ground-based hyperspectral data for plant nitrogen concentration estimation in rice. Frontiers in Plant Science, 9, 1–13. https://doi.org/10.3389/fpls.2018.00936
- Zhou, X., Zhao, C., Sun, J., Yao, K., & Xu, M. (2023). Detection of lead content in oilseed rape leaves and roots based on deep transfer learning and hyperspectral imaging technology. Spectrochimica Acta - Part A: Molecular and Biomolecular Spectroscopy, 290, Article 122288. https://doi.org/10.1016/j.saa.2022.122288